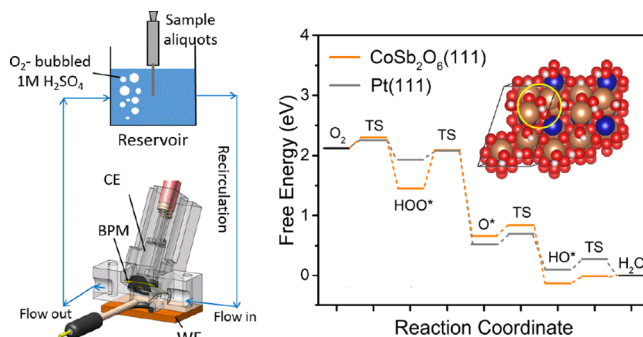


Stability and Activity of Cobalt Antimonate for Oxygen Reduction in Strong Acid

Lan Zhou,[§] Hao Li,[§] Yungchieh Lai, Matthias Richter, Kevin Kan, Joel A. Haber, Sara Kelly, Zhenbin Wang, Yubing Lu, R. Soyoung Kim, Xiang Li, Junko Yano, Jens K. Nørskov,^{*} and John M. Gregoire^{*}

ABSTRACT: Guided by computational Pourbaix screening and high-throughput experiments aimed at the development of precious-metal-free fuel cells, we investigate rutile CoSb_2O_6 as an electrocatalyst for oxygen reduction in 1 M sulfuric acid. Following 4 h of catalyst conditioning at 0.7 V vs RHE, operation at this potential for 20 h yielded an average current density of -0.17 mA cm^{-2} with corrosion at a rate of $0.04 \text{ nm hour}^{-1}$ that is stoichiometric with catalyst composition. Surface Pourbaix analysis of the (111) surface identified partial H coverage under operating conditions. The Sb active site has an HO^* binding free energy of 0.49 eV, which is near the peak of the kinetic $4e^-$ ORR volcano for transition-metal oxides in acidic conditions. The experimental demonstration of operational stability and computational identification of a reaction pathway with favorable energetics place rutile CoSb_2O_6 among the most promising precious-metal-free electrocatalysts for oxygen reduction in acidic media.



The development of active and stable catalysts for electrochemical reactions in harsh corrosive environments, such as strong acidic media under high electrochemical potentials, is a challenge at the forefront of electrochemistry for clean energy technologies. Platinum-based materials remain the state-of-the-art for catalyzing the oxygen reduction reaction (ORR), a half-cell cathode electrochemical reaction essential to energy conversion technologies such as fuel cells and metal–air batteries.^{1–8} However, the limitations due to the inherent scarcity and expense of precious metals have been compounded by insufficient operational durability. Broad deployment of these technologies hinges upon development of active, corrosion-resistant, and earth-abundant electrocatalysts for the ORR, prompting the community’s investigation of transition-metal alloys and intermetallics; carbon-supported transition metal/nitrogen catalysts (Fe-, or Co–N/C); and transition-metal oxides, nitrides, carbides, oxynitrides, carbonitrides, phosphides, and chalcogenides.^{3,6,9–28} Although some platinum-group-metal (PGM)-free Fe–N–C electrocatalysts have exhibited ORR activities approaching that of commercial Pt/C electrocatalysts,²⁹ to date these materials show limited stability and durability against chemical/electrochemical attack under the strong acidic conditions required for incorporation in proton exchange membrane fuel cells.

Using computational Pourbaix diagrams, a family of rutile transition-metal antimonate phases, MSb_2O_6 ($M = \text{Mn, Fe, Co, Ni}$), were among 68 oxide materials recently identified as Pourbaix-stable in potential ranges relevant for oxygen electrochemistry in a strong acid electrolyte.^{22,30} Several transition-metal antimonates have been investigated experimentally as electrocatalysts for OER^{31–34} and the chlorine evolution reaction (CER).^{33,35} Among them, CoSb_2O_6 exhibited a reasonable OER activity under acidic conditions as well as a high corrosion resistance under both OER and CER, in agreement with the theoretical results.^{22,30} Initial studies indicate that CoSb_2O_6 is stable and active for ORR in alkaline electrolytes,³⁶ and herein we explore Co–Sb oxides for ORR in 1 M H_2SO_4 .

Exploration of MnSb_2O_6 -based OER catalysts revealed that Ni substitution³¹ or Mn enrichment³² on the cation sublattice of the rutile structure greatly enhances activity. Given this

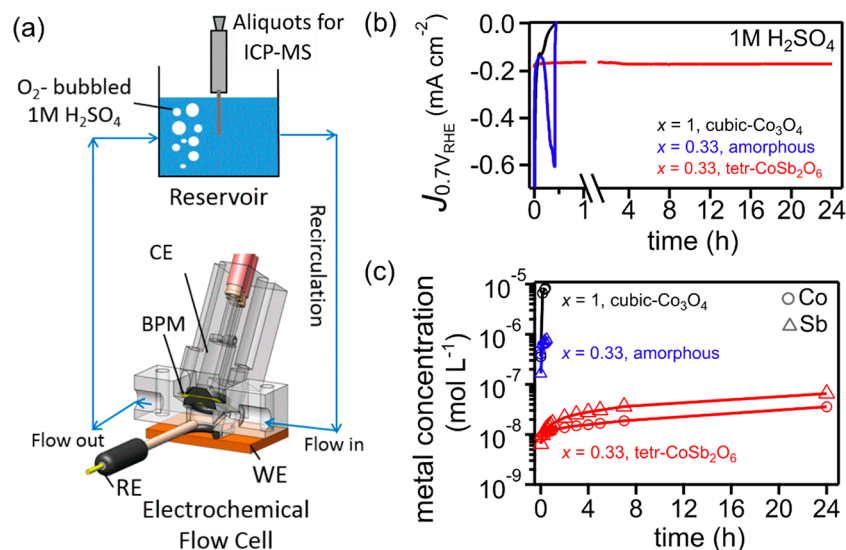


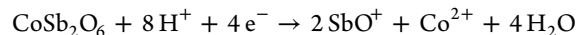
Figure 1. Electrochemical characterization of rutile CoSb_2O_6 ORR activity and stability in 1 atm O_2 -saturated 1 M H_2SO_4 electrolyte. (a) Electrochemical recirculation flow cell where a bipolar membrane (BPM) separates the counter electrode (CE) from the working electrode (WE) chamber that contains the Ag/AgCl reference electrode (RE). Recirculation of electrolyte enables equilibration of the operating catalyst with dissolved metals. Aliquots from the electrolyte reservoir are characterized by ICP-MS to measure the concentration of metals in the electrolyte. (b) The current density at 0.7 V vs RHE over 24 h is shown from the rutile CoSb_2O_6 electrode. The analogous result for a spinel- Co_3O_4 electrode is shown as a baseline with measurement terminated once the current density decayed to zero. (c) The measured metals concentration in electrolyte by ICP-MS over the course of the measurements in panel b.

precedent, catalyst screening in the present work commenced with combinatorial investigation of the phase behavior, activity, and stability of $\text{Co}_x\text{Sb}_{1-x}$ oxides, revealing that unlike MnSb_2O_6 for OER, the most promising catalyst for ORR is stoichiometric CoSb_2O_6 annealed at 700 °C (see the Supporting Information, Figures S1–S4). The activity and durability was evaluated with 24 h electrolysis in a recirculating electrolyte (Figure 1a) from which aliquots at various time points were used to characterize the evolution of concentration of metals in electrolyte during operation (Figures 1b,c and S5). Cathodic current was observed throughout the 24 h measurement (Figure 1b), with a total cathodic charge density of 14.5 C cm^{-2} , for which ORR is the only plausible explanation. Characterization of the ORR onset potential is provided in Figure S6, where comparison of cyclic voltammograms with N_2 and O_2 -saturated electrolyte indicates that the ORR current is differentiated from the capacitive current at approximately 0.85 V vs RHE.

The primary gradient in the dissolved metals concentrations occurs within 4 h of electrolysis (Figure 1c), at which time the concentrations of Sb and Co are approximately 3×10^{-8} and $1.5 \times 10^{-8} \text{ mol L}^{-1}$, respectively. Each of these concentrations increases by approximately 2 \times over the next 20 h, indicating a finite corrosion rate that is stoichiometric with the as-synthesized catalyst composition. Given the electrolyte volume (starting at 50 mL and decreasing by 2 mL for each aliquot), electrode area, and molar volume of CoSb_2O_6 , the average corrosion rate over the first 4 h and the final 20 h of catalyst operation is 0.25 and 0.04 nm hour $^{-1}$, respectively. The average current density over this period is -0.17 mA cm^{-2} . To check for precious metal contamination of the electrochemical cell, measurements of the dissolved Pt in the electrolyte were $4 \times 10^{-11} \text{ mol L}^{-1}$ at the beginning of the measurement and $1 \times 10^{-10} \text{ mol L}^{-1}$ at the end of 24 h of electrolysis (Figure S5), which are both within the noise level of the measurement. The Pt underlayer enabled electrical contact to mechanically stable

films, and further confirmation that it does not play a substantial role in the ORR catalysis is provided in Figure S7 where comparable current densities are obtained with a Au underlayer.

The computational Pourbaix diagram^{22,37} for CoSb_2O_6 shows that near or below the operating potential of 0.7 V vs RHE at pH 0, the stable aqueous ionic species are SbO^+ and Co^{2+} ; therefore, assuming the corrosion reaction



the 4 e^- per CoSb_2O_6 formula unit (FU) of corrosion corresponds to an average corrosion current density of $6.9 \times 10^{-6} \text{ mA cm}^{-2}$ over the final 20 h of the measurement, which is a small fraction of the observed current density. Assuming the remainder of the current density results from 4 e^- ORR, the Faradaic efficiency toward ORR is approximately 99.99%, with each corroded FU supporting more than 6×10^4 ORR catalytic cycles. By these metrics, CoSb_2O_6 provides a remarkable combination of activity and stability for a PMG-free ORR electrocatalyst operating in strong acid. An initial characterization of the sensitivity of the catalytic activity with respect to dissolved metals concentrations is provided in Figure S8.

For comparison, the electrolysis at 0.7 V vs RHE was performed on a reactive sputtered Co oxide film (Figure 1b,c) that formed a polycrystalline spinel Co_3O_4 with a domain size of 5 nm (Figure S9). The cathodic current drops to zero and the Co concentration in electrolyte approaches $1 \times 10^{-5} \text{ mol L}^{-1}$ within 20 min. Because the concentration of Co in electrolyte never appears to equilibrate with Co_3O_4 in this film, we can infer that the CoSb_2O_6 structure lowers the equilibrium concentration of Co^{2+} by more than 1000 \times . This observation is consistent with computational Pourbaix energetics at pH 0 and 0.7 V vs RHE, which indicate that the rutile CoSb_2O_6 phase is stable at Co^{2+} concentration as low as $1 \times 10^{-9} \text{ mol L}^{-1}$, which is comparable to the $10^{-8} \text{ mol L}^{-1}$ level observed in our experiments, while Co_3O_4 is predicted to dissolve as Co^{2+}

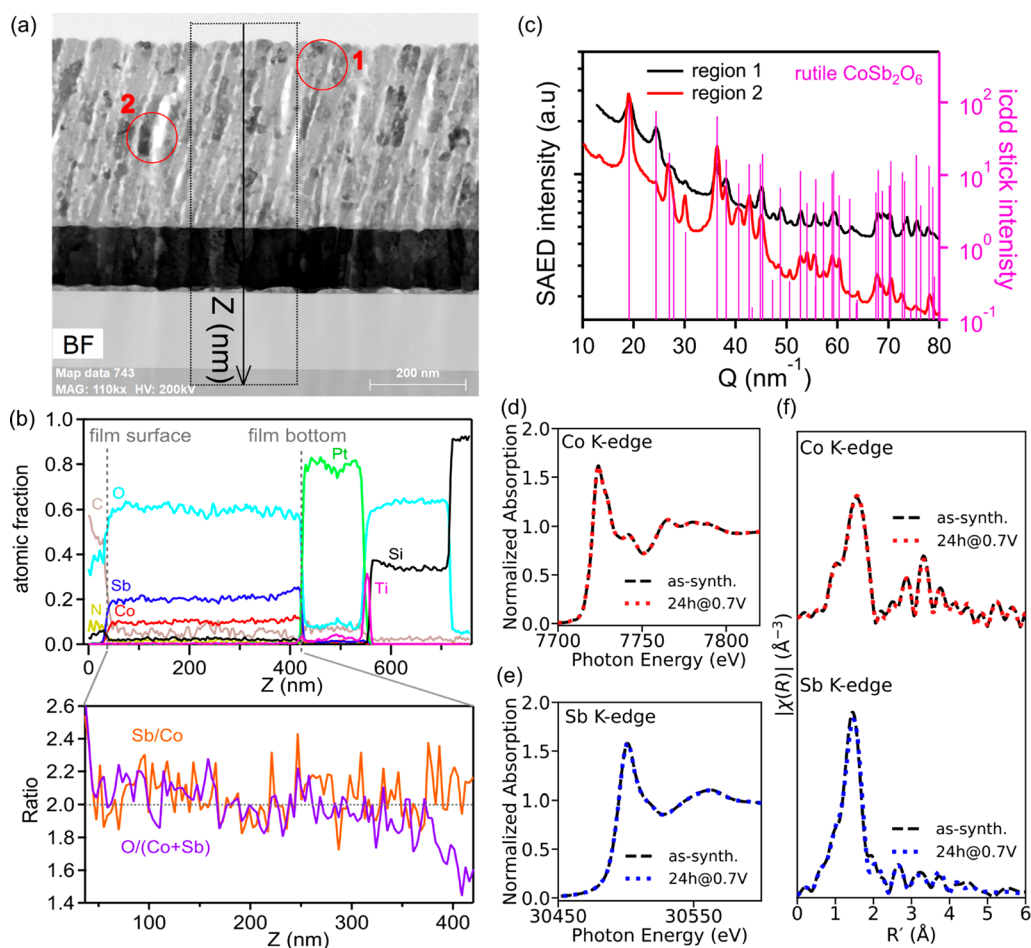


Figure 2. Transmission electron microscopy (TEM) and X-ray absorption spectroscopy (XAS) characterization of the thin-film CoSb_2O_6 electrocatalyst after 24 h of operation at 0.7 V vs RHE in 1 atm O_2 -saturated 1 M H_2SO_4 electrolyte. (a) The bright field image exhibits a columnar thin film with ca. 20 nm grains. (b) The depth profile of elemental concentrations demonstrates negligible interdiffusion with the metal contact layer, and the Sb/Co and O/(Co + Sb) remain within the uncertainty of the formula unit value throughout the ca. 400 nm thickness of the film. (c) The selected area electron diffractions (SAED) from 2 representative regions match the rutile CoSb_2O_6 structure with lattice constants $a = 4.654$ and $c = 3.094$ Å. (d) Co K-edge XANES, (e) Sb K-edge XANES, and (f) the respective EXAFS signals are compared for 2 CoSb_2O_6 electrodes, an as-synthesized electrode, and the electrode from panel a that was operated for 24 h at 0.7 V vs RHE. The consistency of the XANES and EXAFS patterns highlights the chemical and structural stability of the catalyst.

even with concentrations as high as 1 mol L^{-1} .³⁸ To confirm the importance of crystallization into the rutile structure, a sputter-deposited thin film of the same compositions but without annealing was confirmed to be X-ray amorphous and tested at 0.7 V vs RHE where dissolved metals concentrations were 40× larger than the rutile CoSb_2O_6 catalyst, leading to loss of cathodic current after 26 min (Figure 1b,c).

To compare CoSb_2O_6 with recent reports of nonprecious metal electrocatalysts in terms of activity and stability (Table S1), we commence with consideration of molybdenum nitride and molybdenum oxynitride electrocatalysts that were studied for the acidic ORR with monitoring of metal dissolution by inductively coupled plasma optical emission spectrometry (ICP-OES).^{39,40} While MoN exhibits ORR activity at 0.7 V vs RHE that is similar to that of CoSb_2O_6 in the present work, the dissolution rate is 100× higher.³⁹ Group 4 and 5 metal oxides/nitrides/oxynitrides (Ti, Zr, Ta, Nb, Hf, etc.) have been extensively studied as precious-metal-free ORR-active catalysts because of the intrinsic Pourbaix stability of the surface oxides.⁴¹ For example, the solubility of dissolved metal was measured to be $3.5 \times 10^{-7} \text{ mol L}^{-1}$ for a TiO_x catalyst in 0.1 M H_2SO_4 at 50 °C⁴³ and $3.5 \times 10^{-6} \text{ mol L}^{-1}$ in 1 M H_2SO_4 at 70

°C for a ZrO_x catalyst.⁴⁴ These catalysts pose a challenge of simultaneously realizing activity and stability, as evidenced by the ZrO_x catalyst on glassy carbon exhibiting cathodic current density below $5 \mu\text{A cm}^{-2}$ at 0.7 V vs RHE.⁴⁴ Optimization of catalyst electrodes by using conductive graphitic carbon materials,^{42,45–47} controlling the nanoparticle size,⁴⁸ and/or increasing the oxygen vacancy density^{49–51} can increase the cathodic current density up to 0.2 mA cm^{-2} at 0.7 V vs RHE. The CoSb_2O_6 catalyst of the present work (at ambient temperature) exhibits 30× higher current density with 100× lower dissolved metal concentration compared to ZrO_x on glassy carbon, motivating further study of whether analogous optimization of electrode synthesis could elevate the current density of CoSb_2O_6 -based catalysts.

Further characterization of the CoSb_2O_6 catalyst commenced with transmission electron microscopy (TEM) of the electrode after 24 h of electrolysis, revealing a film with low void density and low surface roughness (Figure 2a). The elemental mapping indicates that Co and Sb are distributed uniformly in the thin film with no indication of phase segregation (Figure S10). The measured depth profile of the composition matches the formula unit composition within

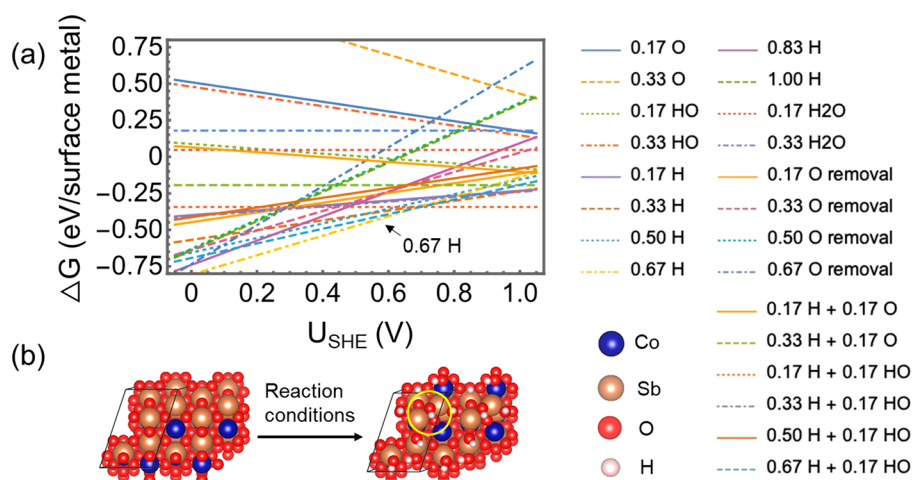


Figure 3. (a) Calculated surface Pourbaix energetics of CoSb₂O₆(111) at pH 0. Each surface is labeled by the fractional monolayer coverage of the indicated species. (b) The metal-terminated CoSb₂O₆(111) surface is shown, as well as the 0.67 H surface identified in panel a to be the operational surface below 0.7 V vs RHE. Brown, blue, red, and pink spheres represent Sb, Co, O, and H, respectively. The yellow circle represents the identified active Sb-site for ORR.

uncertainty throughout the thickness of the film, corroborating the observation of stoichiometric dissolution of Sb and Co (Figure 2b). The apparent crystal domain size of 20 nm is commensurate with the X-ray diffraction (XRD) analysis, as is the selected area electron diffraction (SAED; images are shown in Figure S11) from which more than 20 reflections can be indexed to the rutile structure. The integrated electron diffraction spectra in Figure 2c suggest partial trirutile ordering, as evidenced by relatively low intensity (002) and (101) reflections at 13.5 and 15.09 nm⁻¹, respectively. The intensity of these trirutile-ordering peaks is below the detectability limit by XRD (Figure S3), demonstrating that the majority of the crystalline grains are best characterized by the rutile structure with lattice constants $a = 4.654$ Å and $c = 3.094$ Å. Comparison with an as-synthesized electrode demonstrates that the film morphology is unchanged by the 24 h of electrolysis of Figure 1 (Figure S12). These results were further corroborated by X-ray fluorescence (XRF, Figure S13) as well as X-ray absorption near edge structure (XANES, Figure 2d,e) and extended X-ray absorption fine structure (EXAFS, Figure 2f) characterization at both the Co K-edge and the Sb K-edge. These results indicate no change in bulk composition, oxidation state, or local structure from the 24 h of electrolysis. The XANES and EXAFS patterns are compared to binary oxide standards in Figure S14.

X-ray photon spectroscopy (XPS) characterization (Figure S15) of the same sample indicates that the near-surface region of the thin film catalyst (after exposure to air and XPS measurement at ultrahigh-vacuum conditions) exhibits mixed-valency of both Co and Sb compared to the formal Sb⁵⁺ and Co²⁺ cations of the rutile structure. While these XPS measurements do not characterize the oxidation states of Sb and Co under ORR conditions, comparison of the XPS data with those of a duplicate film with no electrochemical operation reveals no noticeable difference (Figure S15). The combined ICP-MS, TEM, XRF, and XPS characterizations thus indicate that the rutile CoSb₂O₆ film does not develop a passivation layer of different stoichiometry during ORR operation. The catalyst activity drops at the beginning of the measurement and then recovers as the concentrations in electrolyte equilibrate and reach the same Sb:Co stoichiometry

as the catalyst (Figure 1c). The demonstration of stoichiometric corrosion and stable current density is important for guiding investigation of the active site.

Motivated by the computational bulk thermodynamic stability²² and experimental demonstration of stable catalysis, spin-polarized density functional theory calculations with strong on-site Coulomb interaction of localized electrons (DFT+U) were performed to calculate the surface Pourbaix energetics of the surfaces of rutile CoSb₂O₆. The metal-terminated (111) facet was considered for calculations because of its relatively low surface energy (0.068 eV/Å², see Table S2). It can be seen in the surface Pourbaix diagram constructed at pH 0 (Figure 3a) that CoSb₂O₆(111) is partly covered by H* at the O-sites under acidic ORR conditions. The surface with H-coverage of 0.67 monolayer (ML), as illustrated in Figure 3b, is the most stable surface when the potential is at or below 0.7 V vs RHE, indicating that the operational catalyst surface is partially covered by HO* under the acidic ORR conditions. Similar results can be found in facets such as CoSb₂O₆(110), as shown in Figure S16. The surface Pourbaix analysis of Figure 3a also corroborates the bulk thermodynamic analysis that suggested operational stability of CoSb₂O₆; all surfaces involving lattice O removal exhibit relatively high energetics, demonstrating that several surface configurations are more favorable than those leading to corrosion.

Activity analysis based upon the Pourbaix-stable surface reveals that the Sb site of CoSb₂O₆(111), which is circled in Figure 3b, has favorable energetics for the acidic ORR. Figure 4a compares the DFT-calculated free energy diagram for the 4 e⁻ ORR at this site to that of the state-of-art ORR catalyst, Pt, under applied potential of 0.7 V vs RHE (with estimated transition states using the method described in refs 21 and 52). On Pt(111), the reaction proceeds with relatively facile energetics with the removal of HO* as the rate-limiting step. The rate-limiting step on CoSb₂O₆(111) is the dissociation of the HO–O bond because of the relatively weak O-bonding at metal oxide surfaces.²¹

Considering the Pourbaix-stable (0.67 ML H-covered) state of surface under reaction conditions, the calculated HO* binding free energy (G_{HO^*}), which is the primary descriptor for ORR activity, of CoSb₂O₆(111) is 0.49 eV. As illustrated in

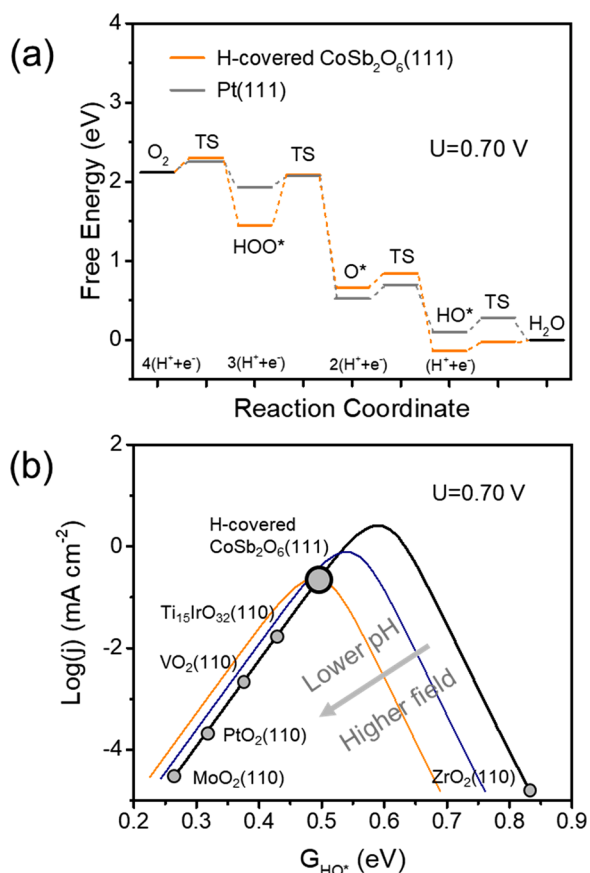


Figure 4. (a) Free-energy diagram for the four-electron ($4e^-$) ORR process on Pt and $\text{CoSb}_2\text{O}_6(111)$ surfaces under applied potential of 0.7 V vs RHE, where HOO^* , O^* , and HO^* are intermediates involved in $4e^-$ ORR path and TS indicates each transition state. (b) Kinetic volcano model for the $4e^-$ ORR at 0.7 V vs RHE. The black plot shows the model of rate vs HO binding free energy (G_{HO^*}) at the potential of zero charge where there are no electric field effects in the energies of transition states and intermediates.²¹ The colored curves show qualitatively the shift in the volcano for increasing electric field, which emulates the effect of decreasing pH. Among known catalysts, $\text{CoSb}_2\text{O}_6(111)$ has a unique G_{HO^*} that makes it especially well-suited for the acidic ORR.

Figure 4b, this value is near the peak of the kinetic $4e^-$ ORR volcano for transition-metal oxides at acidic conditions.²¹ As we recently reported, the low pH leads to a left-and-down shift of the ORR volcano for metal oxides, resulting in a theoretical maximum in activity at relatively strong HO-bonding. Detailed discussions related to pH and field effects on the shift of the ORR volcano can be found in our recent study.²¹ While further characterization of the operational catalyst and assessment of durability at longer time scales and higher temperatures remain important for further development of CoSb_2O_6 -based catalysts for the acidic ORR, the seminal demonstration of CoSb_2O_6 operation with low dissolved metals concentration and low corrosion rate transforms the path toward precious-metal-free fuel cells.

METHODS

Experimental Methods. $\text{Co}_x\text{Sb}_{1-x}\text{O}_z$ composition libraries were fabricated atop 100 mm diameter Pt/Ti/SiO₂/Si substrate by reactive cosputtering of Co and Sb metal sources using 137 and 55 W radio frequency (RF) power supplies,

respectively. The deposition proceeded in a mixed O₂ (0.9 mTorr) and Ar (5.1 mTorr) with 10^{-8} mTorr base pressure, followed by a postdeposition anneal in a box oven at 700 °C in air for 3 h. In addition, a Co oxide library was deposited on a 100 mm diameter FTO-coated glass (Tec-15) substrate using Co source at 140 W without additional postdeposition anneal.

Electrochemical characterization was performed using a scanning drop cell⁵³ for Figures S1-S2. The longer-duration experiments were conducted with a geometric working electrode area of 0.31 cm² defined by the O-ring in a customized recirculation flow cell.⁵⁴ Over the course of CA at 0.7 V vs RHE in 1 atm O₂-saturated 1 M H₂SO₄ aqueous electrolyte, aliquots of electrolyte (2 mL) at various time points were extracted to quantify the dissolved metal concentrations via inductively coupled plasma mass spectrometry (ICP-MS).

The metal oxide compositions were characterized by X-ray fluorescence (XRF) using an EDAX Orbis Micro-XRF system to obtain Co, Sb metal contents, and values of $x = \text{Co}/(\text{Co} + \text{Sb})$ with ca. 1 at. % relative uncertainty. The oxygen signal and thus stoichiometry are not detectable by the XRF experiment.

The bulk crystal structure and phase distribution of composition libraries were determined by X-ray diffraction (XRD) using a Bruker Discover D8 diffractometer with Cu K α radiation from a Bruker I μ S source. The X-ray spot size was limited to a 2 mm length scale, over which the composition is constant to within approximately 1–2 at. %.

X-ray photoelectron spectroscopy (XPS) spectra were measured to determine the near-surface chemistry using a Kratos Axis Ultra instrument with excitation from a monochromatized Al K α radiation at 150 W (10 mA at 15 kV). The collected spectra were calibrated to the carbon 1s peak of 284.8 eV.

To prepare a cross-sectional transmission electron microscopy (TEM) specimen in the specific region tested for 24 h electrolysis, an FEI DualBeam focused ion beam/scanning electron microscope was used, and the sample was capped carbon/I–C prior to milling. TEM experiments were carried out in an FEI Tecnai Osiris FEG/TEM instrument operated at 200 kV in bright-field (BF) and high-resolution (HR) TEM mode. Selected area electron diffraction (SAED) patterns were taken using the same machine. The energy-dispersive X-ray spectroscopy (EDX) elemental mapping was acquired using Bruker Quantax. This characterization was performed by Eurofins EAG Precision TEM in Santa Clara, California.

X-ray absorption spectra (XAS) at the Sb K-edge (30491 eV) were recorded at the Stanford Synchrotron Radiation Lightsource (SSRL, California, United States) at wiggler beamline 7-3, using a liquid-nitrogen-cooled Si(220) $\phi = 0^\circ$ double-crystal monochromator. The storage ring was operated at 3 GeV with a ring current of 494–500 mA in top-up mode. The incident X-rays were monochromatized using a Si(220) double-crystal monochromator which was detuned to 20% of flux maximum at the Sb K-edge to minimize the higher harmonics. The intensity of the incident and transmitted X-rays was monitored using Ar-filled ion chambers. The CoSb_2O_6 samples were measured in fluorescence mode using a 30-element Ge detector (Canberra). An Sb reference (Sb foil) was scanned simultaneously with each sample for energy calibration. Monochromator energy calibration was done using Sb foil spectrum by setting the first inflection point at 30491.0 eV. The XAS measurements at the Co K-edge (7709 eV) spectra were performed at the SSRL at beamline 9-3. Beamline

9-3 is a 16-pole, 2 T wiggler side station with a vertically collimating mirror for harmonic rejection and a cylindrically bent mirror for focusing. The photon energy was selected using a liquid-nitrogen-cooled, double-crystal Si(220) $\phi = 0^\circ$ monochromator. The XAS scans were performed in a continuous scan mode and recorded in fluorescence mode using N₂-filled ion chambers and a PIPS/Lytle detector. A Co reference (Co foil) was scanned simultaneously with each sample for energy calibration. Monochromator energy calibration was done using Co foil spectrum by setting the first inflection point at 7709.0 eV.

An inductively coupled plasma mass spectrometry (ICP-MS) instrument by Thermo Fisher Scientific iCAP RQ was used to determine the concentration of dissolved metals in electrolyte used for electrochemistry at different durations over the course of electrochemical measurements, including Co, Sb, and Pt.

Computational Methods. Spin-polarized DFT+U calculations were conducted using the VASP code, with the U_{eff} for Co acquired from the *Materials Project*.³⁷ The valence electrons were described by expanding the Kohn–Sham wave functions in a plane-wave basis set.⁵⁵ The kinetic energy cutoff was set to 400 eV. The core electrons were treated by the projector augmented-wave (PAW) method.⁵⁶ The electronic exchange and correlations were described by the generalized gradient approximation (GGA) method and the revised functional of Perdew, Burke, and Ernzerhof (RPBE).⁵⁷ A $(3 \times 3 \times 1)$ k-point mesh was used to sample the Brillouin zone. Convergence was defined after the forces of each atom fell below 0.05 eV/Å. The surface Pourbaix diagram calculations were described in our previous study.²¹ The HO* binding free energy was calculated using the total energies of H₂O and H₂ as the references. The zero-point energy, entropic, and solvation energy corrections were acquired from refs 58 and 59.

■ AUTHOR INFORMATION

Corresponding Authors

Jens K. Nørskov – *Catalysis Theory Center, Department of Physics, Technical University of Denmark, 2800 Lyngby, Denmark*; Email: jkno@dtu.dk

John M. Gregoire – *Division of Engineering and Applied Science, California Institute of Technology, Pasadena, California 91125, United States*; orcid.org/0000-0002-2863-5265; Email: gregoire@caltech.edu

Authors

Lan Zhou – *Division of Engineering and Applied Science, California Institute of Technology, Pasadena, California 91125, United States*

Hao Li – *Catalysis Theory Center, Department of Physics, Technical University of Denmark, 2800 Lyngby, Denmark*; orcid.org/0000-0002-7577-1366

Yungchieh Lai – *Division of Engineering and Applied Science, California Institute of Technology, Pasadena, California 91125, United States*

Matthias Richter – *Division of Engineering and Applied Science, California Institute of Technology, Pasadena, California 91125, United States*; orcid.org/0000-0003-0091-2045

Kevin Kan – *Division of Engineering and Applied Science, California Institute of Technology, Pasadena, California 91125, United States*

Joel A. Haber – *Division of Engineering and Applied Science, California Institute of Technology, Pasadena, California 91125, United States*; orcid.org/0000-0001-7847-5506

Sara Kelly – *Department of Chemical Engineering, Stanford University, Stanford, California 94305, United States*

Zhenbin Wang – *Catalysis Theory Center, Department of Physics, Technical University of Denmark, 2800 Lyngby, Denmark*

Yubing Lu – *Molecular Biophysics and Integrated Bioimaging Division, Lawrence Berkeley National Laboratory, Berkeley, California 94720, United States*

R. Soyoung Kim – *Chemical Sciences Division, Lawrence Berkeley National Laboratory, Berkeley, California 94720, United States*

Xiang Li – *SLAC National Accelerator Laboratory, Menlo Park, California 94025, United States*

Junko Yano – *Molecular Biophysics and Integrated Bioimaging Division, Lawrence Berkeley National Laboratory, Berkeley, California 94720, United States*; orcid.org/0000-0001-6308-9071

Author Contributions

[§]L.Z. and H.L. contributed equally to this work.

Notes

The authors declare no competing financial interest.

■ ACKNOWLEDGMENTS

This work was supported by Toyota Research Institute. Use of the Stanford Synchrotron Radiation Lightsource, SLAC National Accelerator Laboratory, is supported by the U.S. Department of Energy, Office of Science, Office of Basic Energy Sciences under Contract No. DE-AC02-76SF00515.

■ REFERENCES

- (1) Gasteiger, H. A.; Kocha, S. S.; Sompalli, B.; Wagner, F. T. Activity Benchmarks and Requirements for Pt, Pt-Alloy, and Non-Pt Oxygen Reduction Catalysts for PEMFCs. *Applied Catalysis B: Environmental* **2005**, *56* (1), 9–35.
- (2) Kang, J.-H.; Lee, J.; Jung, J.-W.; Park, J.; Jang, T.; Kim, H.-S.; Nam, J.-S.; Lim, H.; Yoon, K. R.; Ryu, W.-H.; Kim, I.-D.; Byon, H. R. Lithium–Air Batteries: Air-Breathing Challenges and Perspective. *ACS Nano* **2020**, *14* (11), 14549–14578.
- (3) Stacy, J.; Regmi, Y. N.; Leonard, B.; Fan, M. The Recent Progress and Future of Oxygen Reduction Reaction Catalysis: A Review. *Renewable and Sustainable Energy Reviews* **2017**, *69*, 401–414.
- (4) Debe, M. K. Electrocatalyst Approaches and Challenges for Automotive Fuel Cells. *Nature* **2012**, *486* (7401), 43–51.
- (5) Wu, J.; Yang, H. Platinum-Based Oxygen Reduction Electrocatalysts. *Acc. Chem. Res.* **2013**, *46* (8), 1848–1857.
- (6) Shao, M.; Chang, Q.; Dodelet, J.-P.; Chenitz, R. Recent Advances in Electrocatalysts for Oxygen Reduction Reaction. *Chem. Rev.* **2016**, *116* (6), 3594–3657.

- (7) Sui, S.; Wang, X.; Zhou, X.; Su, Y.; Riffat, S.; Liu, C. A Comprehensive Review of Pt Electrocatalysts for the Oxygen Reduction Reaction: Nanostructure, Activity, Mechanism and Carbon Support in PEM Fuel Cells. *Journal of Materials Chemistry A* **2017**, *5* (5), 1808–1825.
- (8) Kongkanand, A.; Mathias, M. F. The Priority and Challenge of High-Power Performance of Low-Platinum Proton-Exchange Membrane Fuel Cells. *J. Phys. Chem. Lett.* **2016**, *7* (7), 1127–1137.
- (9) Jaouen, F.; Proietti, E.; Lefevre, M.; Chenitz, R.; Dodelet, J.-P.; Wu, G.; Chung, H. T.; Johnston, C. M.; Zelenay, P. Recent Advances in Non-Precious Metal Catalysis for Oxygen-Reduction Reaction in Polymer Electrolyte Fuel Cells. *Energy Environ. Sci.* **2011**, *4* (1), 114–130.
- (10) Shao, M. Palladium-Based Electrocatalysts for Hydrogen Oxidation and Oxygen Reduction Reactions. *J. Power Sources* **2011**, *196* (5), 2433–2444.
- (11) Ben Liew, K.; Daud, W. R. W.; Ghasemi, M.; Leong, J. X.; Su Lim, S.; Ismail, M. Non-Pt Catalyst as Oxygen Reduction Reaction in Microbial Fuel Cells: A Review. *Int. J. Hydrogen Energy* **2014**, *39* (10), 4870–4883.
- (12) Banham, D.; Ye, S.; Pei, K.; Ozaki, J.; Kishimoto, T.; Imashiro, Y. A Review of the Stability and Durability of Non-Precious Metal Catalysis for the Oxygen Reduction Reaction in Proton Exchange Membrane Fuel Cells. *J. Power Sources* **2015**, *285*, 334–348.
- (13) Hong, W. T.; Risch, M.; Stoerzinger, K. A.; Grimaud, A.; Suntivich, J.; Shao-Horn, Y. Toward the Rational Design of Non-Precious Transition Metal Oxides for Oxygen Electrocatalysis. *Energy Environ. Sci.* **2015**, *8* (5), 1404–1427.
- (14) Kulkarni, A.; Siahrostami, S.; Patel, A.; Nørskov, J. K. Understanding Catalytic Activity Trends in the Oxygen Reduction Reaction. *Chem. Rev.* **2018**, *118* (5), 2302–2312.
- (15) Wang, Y.; Li, J.; Wei, Z. Transition-Metal-Oxide-Based Catalysts for the Oxygen Reduction Reaction. *J. Mater. Chem. A* **2018**, *6* (18), 8194–8209.
- (16) Li, Y.; Li, Q.; Wang, H.; Zhang, L.; Wilkinson, D. P.; Zhang, J. Recent Progresses in Oxygen Reduction Reaction Electrocatalysts for Electrochemical Energy Applications. *Electrochem. Energy Rev.* **2019**, *2* (4), 518–538.
- (17) Ma, R.; Lin, G.; Zhou, Y.; Liu, Q.; Zhang, T.; Shan, G.; Yang, M.; Wang, J. A Review of Oxygen Reduction Mechanisms for Metal-Free Carbon-Based Electrocatalysts. *npj Comput. Mater.* **2019**, *5* (1), 1–15.
- (18) Wang, X.; Li, Z.; Qu, Y.; Yuan, T.; Wang, W.; Wu, Y.; Li, Y. Review of Metal Catalysts for Oxygen Reduction Reaction: From Nanoscale Engineering to Atomic Design. *Chem.* **2019**, *5* (6), 1486–1511.
- (19) Holby, E. F.; Wang, G.; Zelenay, P. Acid Stability and Demetalation of PGM-Free ORR Electrocatalyst Structures from Density Functional Theory: A Model for “Single-Atom Catalyst” Dissolution. *ACS Catal.* **2020**, *10* (24), 14527–14539.
- (20) Zamora Zeledón, J. A.; Kamat, G. A.; Gunasooriya, G. T. K. K.; Nørskov, J. K.; Stevens, M. B.; Jaramillo, T. F. Probing the Effects of Acid Electrolyte Anions on Electrocatalyst Activity and Selectivity for the Oxygen Reduction Reaction. *ChemElectroChem.* **2021**, *8* (13), 2467–2478.
- (21) Li, H.; Kelly, S.; Guevarra, D.; Wang, Z.; Wang, Y.; Haber, J. A.; Anand, M.; Gunasooriya, G. T. K. K.; Abraham, C. S.; Vijay, S.; Gregoire, J. M.; Nørskov, J. K. Analysis of the Limitations in the Oxygen Reduction Activity of Transition Metal Oxide Surfaces. *Nat. Catal.* **2021**, *4* (6), 463–468.
- (22) Wang, Z.; Zheng, Y.-R.; Chorkendorff, I.; Nørskov, J. K. Acid-Stable Oxides for Oxygen Electrocatalysis. *ACS Energy Lett.* **2020**, *5* (9), 2905–2908.
- (23) Seh, Z. W.; Kibsgaard, J.; Dickens, C. F.; Chorkendorff, I.; Nørskov, J. K.; Jaramillo, T. F. Combining Theory and Experiment in Electrocatalysis: Insights into Materials Design. *Science* **2017**, *355* (6321), No. eaad4998.
- (24) Morozan, A.; Josselme, B.; Palacin, S. Low-Platinum and Platinum-Free Catalysts for the Oxygen Reduction Reaction at Fuel Cell Cathodes. *Energy Environ. Sci.* **2011**, *4* (4), 1238–1254.
- (25) Ishihara, A.; Ohgi, Y.; Matsuzawa, K.; Mitsushima, S.; Ota, K. Progress in Non-Precious Metal Oxide-Based Cathode for Polymer Electrolyte Fuel Cells. *Electrochim. Acta* **2010**, *55* (27), 8005–8012.
- (26) Chisaka, M.; Morioka, H. Phosphor and Nitrogen Co-Doped Rutile TiO₂ Covered on TiN for Oxygen Reduction Reaction in Acidic Media. *Catal. Sci. Technol.* **2019**, *9* (3), 611–619.
- (27) Ishihara, A.; Tominaka, S.; Mitsushima, S.; Imai, H.; Sugino, O.; Ota, K. Challenge of Advanced Low Temperature Fuel Cells Based on High Degree of Freedom of Group 4 and 5 Metal Oxides. *Current Opinion in Electrochemistry* **2020**, *21*, 234–241.
- (28) Kong, J.; Cheng, W. Recent Advances in the Rational Design of Electrocatalysts towards the Oxygen Reduction Reaction. *Chinese Journal of Catalysis* **2017**, *38* (6), 951–969.
- (29) Zhang, H.; Hwang, S.; Wang, M.; Feng, Z.; Karakalos, S.; Luo, L.; Qiao, Z.; Xie, X.; Wang, C.; Su, D.; Shao, Y.; Wu, G. Single Atomic Iron Catalysts for Oxygen Reduction in Acidic Media: Particle Size Control and Thermal Activation. *J. Am. Chem. Soc.* **2017**, *139* (40), 14143–14149.
- (30) Gunasooriya, G. T. K. K.; Nørskov, J. K. Analysis of Acid-Stable and Active Oxides for the Oxygen Evolution Reaction. *ACS Energy Lett.* **2020**, *5* (12), 3778–3787.
- (31) Moreno-Hernandez, I. A.; MacFarland, C. A.; Read, C. G.; Papadantonakis, K. M.; Bruntschwig, B. S.; Lewis, N. S. Crystalline Nickel Manganese Antimonate as a Stable Water-Oxidation Catalyst in Aqueous 1.0 M H₂SO₄. *Energy Environ. Sci.* **2017**, *10* (10), 2103–2108.
- (32) Zhou, L.; Shinde, A.; Montoya, J. H.; Singh, A.; Gul, S.; Yano, J.; Ye, Y.; Crumlin, E. J.; Richter, M. H.; Cooper, J. K.; Stein, H. S.; Haber, J. A.; Persson, K. A.; Gregoire, J. M. Rutile Alloys in the Mn–Sb–O System Stabilize Mn³⁺ To Enable Oxygen Evolution in Strong Acid. *ACS Catal.* **2018**, *8* (12), 10938–10948.
- (33) Evans, T. A.; Choi, K.-S. Electrochemical Synthesis and Investigation of Stoichiometric, Phase-Pure CoSb₂O₆ and MnSb₂O₆ Electrodes for the Oxygen Evolution Reaction in Acidic Media. *ACS Appl. Energy Mater.* **2020**, *3* (6), 5563–5571.
- (34) Ham, K.; Hong, S.; Kang, S.; Cho, K.; Lee, J. Extensive Active-Site Formation in Trirutile CoSb₂O₆ by Oxygen Vacancy for Oxygen Evolution Reaction in Anion Exchange Membrane Water Splitting. *ACS Energy Lett.* **2021**, *6* (2), 364–370.
- (35) Moreno-Hernandez, I. A.; Bruntschwig, B. S.; Lewis, N. S. Crystalline Nickel, Cobalt, and Manganese Antimonates as Electrocatalysts for the Chlorine Evolution Reaction. *Energy Environ. Sci.* **2019**, *12* (4), 1241–1248.
- (36) Gunasooriya, G. T. K. K.; Kreider, M. E.; Liu, Y.; Zeledón, J. A. Z.; Wang, Z.; Valle, E.; Yang, A.-C.; Gallo, A.; Sinclair, R.; Stevens, M. B.; Jaramillo, T. F.; Nørskov, J. K. First-Row Transition Metal Antimonates for the Oxygen Reduction Reaction. *ChemRxiv* **2021**, DOI: 10.33774/chemrxiv-2021-rmcq1.
- (37) Jain, A.; Ong, S. P.; Hautier, G.; Chen, W.; Richards, W. D.; Dacek, S.; Cholia, S.; Gunter, D.; Skinner, D.; Ceder, G.; Persson, K. A. Commentary: The Materials Project: A Materials Genome Approach to Accelerating Materials Innovation. *APL Materials* **2013**, *1* (1), 011002.
- (38) Singh, A. K.; Zhou, L.; Shinde, A.; Suram, S. K.; Montoya, J. H.; Winston, D.; Gregoire, J. M.; Persson, K. A. Electrochemical Stability of Metastable Materials. *Chem. Mater.* **2017**, *29* (23), 10159–10167.
- (39) Stevens, M. B.; Kreider, M. E.; Patel, A. M.; Wang, Z.; Liu, Y.; Gibbons, B. M.; Statt, M. J.; Ievlev, A. V.; Sinclair, R.; Mehta, A.; Davis, R. C.; Nørskov, J. K.; Gallo, A.; King, L. A.; Jaramillo, T. F. Identifying and Tuning the In Situ Oxygen-Rich Surface of Molybdenum Nitride Electrocatalysts for Oxygen Reduction. *ACS Appl. Energy Mater.* **2020**, *3* (12), 12433–12446.
- (40) Kreider, M. E.; Stevens, M. B.; Liu, Y.; Patel, A. M.; Statt, M. J.; Gibbons, B. M.; Gallo, A.; Ben-Naim, M.; Mehta, A.; Davis, R. C.; Ievlev, A. V.; Nørskov, J. K.; Sinclair, R.; King, L. A.; Jaramillo, T. F. Nitride or Oxynitride? Elucidating the Composition–Activity

Relationships in Molybdenum Nitride Electrocatalysts for the Oxygen Reduction Reaction. *Chem. Mater.* **2020**, *32* (7), 2946–2960.

(41) Takasu, Y.; Suzuki, M.; Yang, H.; Ohashi, T.; Sugimoto, W. Oxygen Reduction Characteristics of Several Valve Metal Oxide Electrodes in HClO₄ Solution. *Electrochim. Acta* **2010**, *55* (27), 8220–8229.

(42) Seo, J.; Zhao, L.; Cha, D.; Takanabe, K.; Katayama, M.; Kubota, J.; Domen, K. Highly Dispersed TaOx Nanoparticles Prepared by Electrodeposition as Oxygen Reduction Electrocatalysts for Polymer Electrolyte Fuel Cells. *J. Phys. Chem. C* **2013**, *117* (22), 11635–11646.

(43) Kim, J.-H.; Ishihara, A.; Mitsushima, S.; Kamiya, N.; Ota, K.-I. Catalytic Activity of Titanium Oxide for Oxygen Reduction Reaction as a Non-Platinum Catalyst for PEFC. *Electrochim. Acta* **2007**, *52* (7), 2492–2497.

(44) Liu, Y.; Ishihara, A.; Mitsushima, S.; Kamiya, N.; Ota, K. Zirconium Oxide for PEFC Cathodes. *Electrochem. Solid-State Lett.* **2005**, *8* (8), A400.

(45) Chisaka, M.; Itagaki, N. Evaluation and Enhancement of the Oxygen Reduction Reaction Activity on Hafnium Oxide Nanoparticles Assisted by L(+)-Lysine. *Electrochim. Acta* **2016**, *201*, 279–285.

(46) Ishihara, A.; Chisaka, M.; Ohgi, Y.; Matsuzawa, K.; Mitsushima, S.; Ota, K. Synthesis of Nano-TaO_x Oxygen Reduction Reaction Catalysts on Multi-Walled Carbon Nanotubes Connected via a Decomposition of Oxy-Tantalum Phthalocyanine. *Phys. Chem. Chem. Phys.* **2015**, *17* (12), 7643–7647.

(47) Chisaka, M.; Sasaki, H.; Muramoto, H. Monoclinic Hafnium Oxynitride Supported on Reduced Graphene Oxide to Catalyse the Oxygen Reduction Reaction in Acidic Media. *Phys. Chem. Chem. Phys.* **2014**, *16* (38), 20415–20419.

(48) Seo, J.; Cha, D.; Takanabe, K.; Kubota, J.; Domen, K. Particle Size Dependence on Oxygen Reduction Reaction Activity of Electrodeposited TaO_x Catalysts in Acidic Media. *Phys. Chem. Chem. Phys.* **2014**, *16* (3), 895–898.

(49) Lee, N.-W.; Yoon, K. R.; Lee, J.-Y.; Park, Y.; Pyo, S.-J.; Kim, G.-Y.; Ha, D.-H.; Ryu, W.-H. Highly Conductive Off-Stoichiometric Zirconium Oxide Nanofibers with Controllable Crystalline Structures and Bandgaps and Improved Electrochemical Activities. *ACS Appl. Energy Mater.* **2019**, *2* (5), 3513–3522.

(50) Jung, J.-W.; Kim, G.-Y.; Lee, N.-W.; Ryu, W.-H. Low-Temperature Synthesis of Tetragonal Phase of Hafnium Oxide Using Polymer-Blended Nanofiber Precursor. *Appl. Surf. Sci.* **2020**, *533*, 147496.

(51) Madkikar, P.; Menga, D.; Harzer, G. S.; Mittermeier, T.; Siebel, A.; Wagner, F. E.; Merz, M.; Schuppler, S.; Nagel, P.; Muñoz-García, A. B.; Pavone, M.; Gasteiger, H. A.; Piana, M. Nanometric Fe-Substituted ZrO₂ on Carbon Black as PGM-Free ORR Catalyst for PEMFCs. *J. Electrochem. Soc.* **2019**, *166* (7), F3032.

(52) Dickens, C. F.; Kirk, C.; Nørskov, J. K. Insights into the Electrochemical Oxygen Evolution Reaction with Ab Initio Calculations and Microkinetic Modeling: Beyond the Limiting Potential Volcano. *J. Phys. Chem. C* **2019**, *123* (31), 18960–18977.

(53) Gregoire, J. M.; Xiang, C.; Liu, X.; Marcin, M.; Jin, J. Scanning Droplet Cell for High Throughput Electrochemical and Photoelectrochemical Measurements. *Rev. Sci. Instrum.* **2013**, *84* (2), 024102.

(54) Lai, Y.; Jones, R. J. R.; Wang, Y.; Zhou, L.; Gregoire, J. M. Scanning Electrochemical Flow Cell with Online Mass Spectroscopy for Accelerated Screening of Carbon Dioxide Reduction Electrocatalysts. *ACS Comb. Sci.* **2019**, *21* (10), 692–704.

(55) Kohn, W.; Sham, L. J. Self-Consistent Equations Including Exchange and Correlation Effects. *Phys. Rev.* **1965**, *140* (4A), A1133–A1138.

(56) Blöchl, P. E. Projector Augmented-Wave Method. *Phys. Rev. B* **1994**, *50* (24), 17953–17979.

(57) Hammer, B.; Hansen, L. B.; Nørskov, J. K. Improved Adsorption Energetics within Density-Functional Theory Using

Revised Perdew-Burke-Ernzerhof Functionals. *Phys. Rev. B* **1999**, *59* (11), 7413–7421.

(58) Bajdich, M.; García-Mota, M.; Vojvodic, A.; Nørskov, J. K.; Bell, A. T. Theoretical Investigation of the Activity of Cobalt Oxides for the Electrochemical Oxidation of Water. *J. Am. Chem. Soc.* **2013**, *135* (36), 13521–13530.

(59) Gauthier, J. A.; Dickens, C. F.; Chen, L. D.; Doyle, A. D.; Nørskov, J. K. Solvation Effects for Oxygen Evolution Reaction Catalysis on IrO₂(110). *J. Phys. Chem. C* **2017**, *121* (21), 11455–11463.